DOI: 10.1002/ange.200803520

Defect Chemistry

Orientation-Dependent Arrangement of Antisite Defects in Lithium Iron(II) Phosphate Crystals**

Sung-Yoon Chung, Si-Young Choi, Takahisa Yamamoto, and Yuichi Ikuhara*

The distribution and local concentration of point defects in crystal lattices such as dopants and atomic vacancies have been recognized as significant factors that govern the overall electrical and optical properties of inorganic crystals.[1–3] The intentional use of impurities in semiconductors[1] and the formation of ionic vacancies in ion-conducting metal oxides[2] are well-known examples of displaying the correlation between atomic-scale chemical variations and resulting physical properties. Furthermore, as the chemically different environment induced by point defects leads to breaking of the ordered arrangement of atoms in crystals, mass and charge transport behaviors are also considerably affected by the presence of the defects.[4]

In many lithium intercalation compounds, an ordered array of lithium is usually maintained. Therefore, the control of point defects, including cation disorder, is of major significance for application to electrodes in rechargeable batteries. A variety of investigations on lithium vacancies and cation intermixing have been reported for layered oxides.[5] In contrast, few experimental details showing the atomic-scale point defects in olivine-type lithium metal phosphates $LiMPO_4$ (where M = Fe, Mn, Ni, Co), are yet available, although these phosphates have attracted a great deal of attention as alternative cathode materials in lithium-ion batteries over the past decade.[6] As illustrated in Figure 1a, the lithium and the metal (M) ion in $LiMPO_4$ having an ordered olivine structure occupy different octahedral inter-

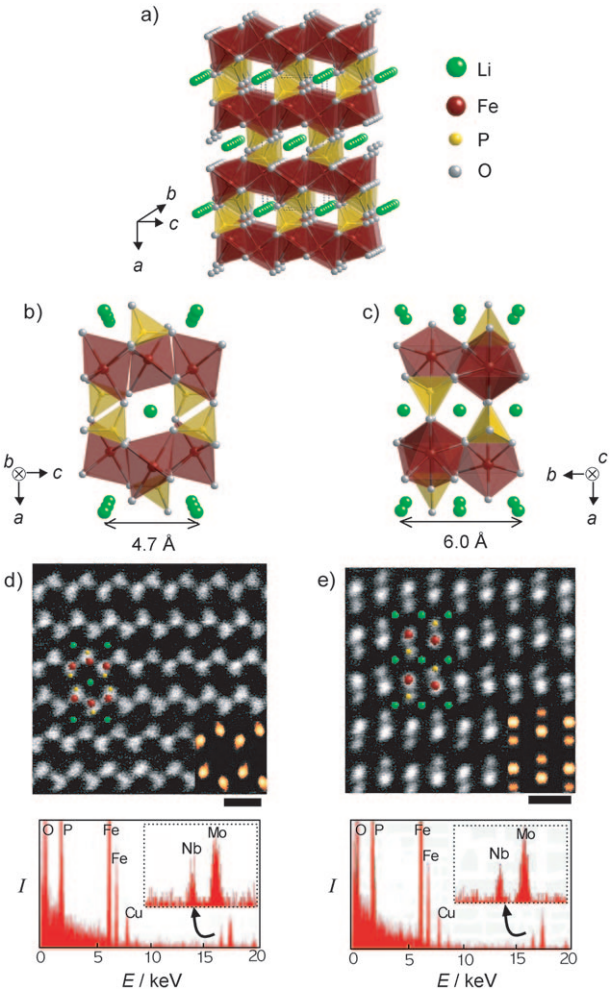

Figure 1. a) Crystal structure of $LiFePO_4$, illustrating well-ordered cation partitioning of Li (green) in M1 sites and Fe (red) in M2 sites. Li green, Fe red, P yellow, and O gray. b, c) Illustrations of a unit cell and d, e) HAADF-STEM images perpendicular to the *b* and *c* axis, respectively. The superimposed atomic arrays on each image indicate the locations of atom columns. The insets in color show simulated HAADF images according to the experimentally obtained image data. The energy dispersive X-ray spectra (bottom) confirm the presence of niobium in the lattice. The scale bars are 5 Å.

[*] Prof. S.-Y. Chung[+]
Department of Materials Science and Engineering, Inha University, Incheon 402-751 (Korea)
and
Nalphates LLC
Wilmington, DE 19801 (USA)
Fax: (+82) 32-862-5546
E-mail: nalphates@gmail.com
E-mail: sychung@inha.ac.kr
Dr. S.-Y. Choi[+]
Korea Institute of Materials Science, Changwon 641-831 (Korea)
and
Institute of Engineering Innovation, University of Tokyo, Tokyo 113-8656 (Japan)
Prof. T. Yamamoto
Department of Advanced Materials Science, University of Tokyo, Tokyo 113-8656 (Japan)
and
Nanostructures Research Laboratory (Japan) Fine Ceramics Center Nagoya 456-8587 (Japan)
Prof. Y. Ikuhara
Institute of Engineering Innovation, University of Tokyo
Tokyo 113-8656 (Japan)
and
Nanostructures Research Laboratory (Japan) Fine Ceramics Center, Nagoya 456-8587 (Japan)
[+] These authors contributed equally to this work.
[**] This research was supported by the Korea Research Foundation, grant no. KRF 2008-331-D00249.
Supporting information for this article is available on the WWW under http://dx.doi.org/10.1002/anie.200803520.

stitial sites in the crystal structure. Lithium is found in the edge-sharing site (M1) and the metal M in the corner-sharing site (M2).[7] Based on the findings of systematic investigation on thermodynamic aspects of defect formation in various olivine-type minerals,[8] cation-exchange antisite defects between M1 and M2 sites are among the most frequently occurring point defects in the crystal structure. Thus, proper control and direct identification of the distribution of these defects in the crystal lattice are crucial steps toward enhancement of effective lithium mobility during the intercalation–deintercalation reaction in olivine phosphates.

Herein, we describe the synthesis of niobium-doped $LiFePO_4$ crystals and directly show that the aggregated antisite defects in lithium sites of the doped $LiFePO_4$ are not dispersed randomly, but are arranged preferentially along the *b* axis. To observe this preferentially arrangement, we utilized high-angle annular dark-field (HAADF) scanning transmission electron microscopy (STEM) with a spherical-aberration corrector. The intensity of atom columns in HAADF images is roughly proportional to the square of the average atomic number (Z).[9] Consequently, the contrast variation in this image mode straightforwardly indicates the difference of chemical composition in individual atom columns. Furthermore, the recent progress of aberration correction in STEM, which offers improved electron beam brightness,[10a] enables the clearer identification of individual atom columns with enhanced spatial resolution.[10] Thus, aberration-corrected HAADF-STEM is a very efficient tool to visualize the lithium columns that contain antisite iron of much higher Z.[11]

As schematically shown in Figure 1 b,c when the crystal structure of orthorhombic $LiFePO_4$ is observed along the two main zone directions of [010] and [001], the ordered arrangement of lithium (green spheres) and iron (red spheres) between M1 and M2 sites in the unit cell can be easily confirmed. The columns containing iron in the M2 sites show the brightest contrast in the HAADF STEM images; however, no visible contrast is found in the lithium columns of M1 sites, as lithium atoms ($Z = 3$) are too light to be detected in the HAADF mode. For direct comparison, the two-dimensional atomic configurations are superimposed on the STEM images in Figure 1 d,e. The projected distance between iron and phosphorous is longer when the image is viewed along the [001] projection (1.93 Å) compared to the image viewed in the [010] projection (1.26 Å). Therefore, the iron (Z = 26) and phosphorous (Z = 15) columns can be clearly resolved in Figure 1 e (projection [001]), showing different relative intensities with each other, while a single image feature is observed for each iron–phosphorous column in Figure 1 d (projection [010]) in accordance with a previous result.[11] Furthermore, it was confirmed during the STEM analysis that aliovalent niobium can be doped in the crystal lattice. The energy dispersive X-ray (EDX) spectra acquired from the regions shown in the HAADF images verify the presence of niobium in the lattice (Figure 1 d,e).[6c] A quantitative analysis using the EDX spectra demonstrates that circa 2.5 at% of niobium is soluble in the lattice. Note that the small peaks for copper and molybdenum arise from a TEM holder and a specimen grid, respectively.

Image simulations based on the multislice method were carried out as a function of the degree of exchange between the M sites to quantitatively investigate the contrast variations of each atomic column in the HAADF images. The insets of the images in Figure 1 d,e are simulated HAADF images without antisite exchange and are in good agreement with the experimentally obtained images. However, as the degree of lithium–iron exchange increases, invisible lithium columns become brighter, showing a detectable intensity. Figure 2 presents two series of simulated HAADF images in the [010] (Figure 2 a) and [001] (Figure 2 b) projections, in

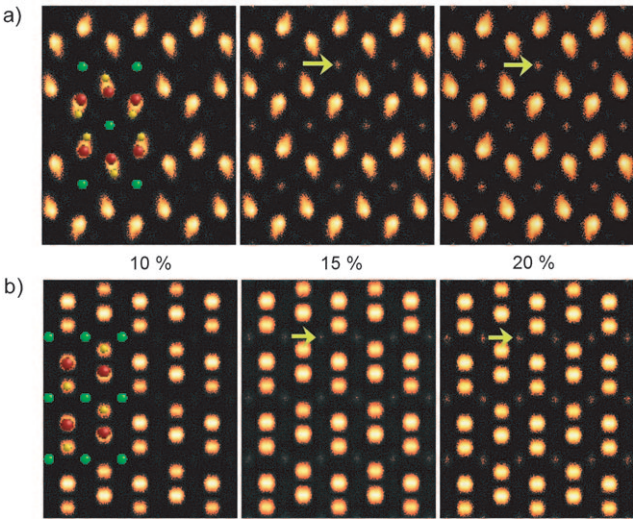

Figure 2. Two series of simulated annular dark-field (ADF) images as a function of the degree of disorder between the M1 and M2 sites in a) [010] and b) [001] projections. The intensities in each image are calculated for 10%, 15%, and 20% lithium–iron exchange. The atomic arrays in each projection are also superimposed. The lithium columns show a sufficiently bright intensity starting from a lithium–iron exchange of 15% (denoted by the arrow).

which lithium–iron exchange occurs up to 20% at the M1 and M2 sites. As indicated by arrows in Figure 2, a bright spot in the lithium columns arise from antisite iron and is detected in both projections if the degree of exchange is 15% or more. Therefore, the local distribution of antisite iron cations in the lithium columns can be effectively probed and visualized by aberration-corrected STEM.

Atomic-resolution *Z*-contrast observations frequently show nanoscale regions that include lithium columns having a white contrast with sufficient intensity in the niobium-doped $LiFePO_4$ crystals, while the overall ordered configurations of the olivine structure are maintained. A typical HAADF image of the [010] projection for the regions and a magnified view in Figure 3 a demonstrate the presence of antisite iron cations in some of the lithium sites. This result indicates that the iron cations occupying the lithium sites are locally aggregated rather than homogeneously distributed in the lattice. This observation is consistent with the previous STEM result.[11] By contrast, it should be noted that almost no detectable white contrast in the lithium sites for the antisite defects was found for HAADF images taken in the [001]

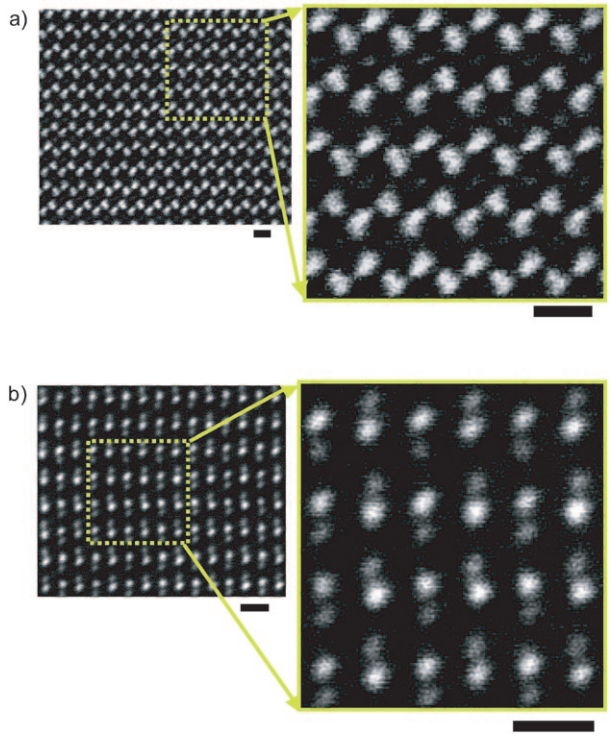

Figure 3. HAADF-STEM images and their enlargements for each region denoted by a green rectangle for niobium-doped $LiFePO_4$ crystals in a) [010] and b) [001] projections. The magnified image in the [010] projection demonstrates that some of the lithium columns have a bright contrast with significant intensity, while maintaining an ordered arrangement of the iron–phosphorous contours. No lithium columns with visible intensity are observed in HAADF images obtained in the [001] projection. The scale bars are 5 Å.

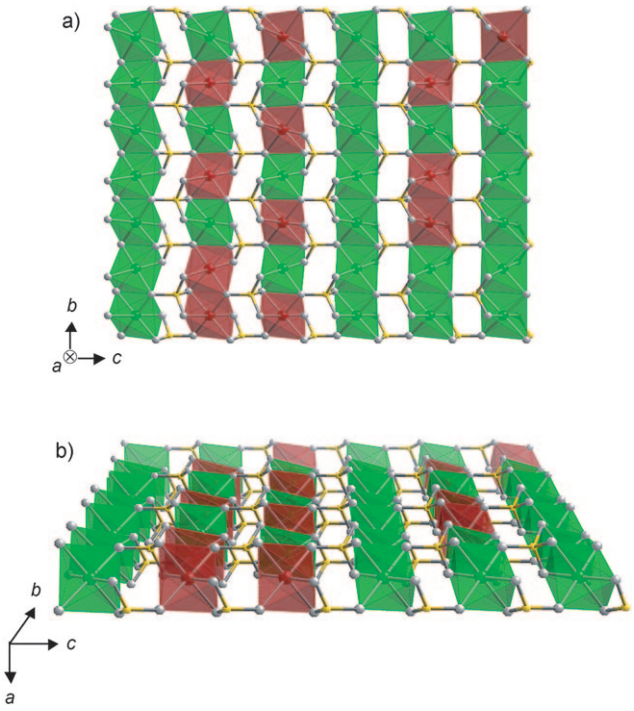

Figure 4. The arrangement of antisite iron cations, showing a preferential arrangement along the *b* axis. a) Two-dimensional description of the edge-sharing M1 octahedral sites of lithium (green) in the *b*–*c* plane, and b) a corresponding three-dimensional view. The antisite iron cation is shown in red.

projection. Although dumbbell-like image features for the iron and phosphorous columns can be clearly discriminated, there are no lithium columns showing a bright contrast in the [001] projection images (Figure 3b). We obtained 15 different HAADF images, each of which shows more than 220 lithium columns, all in the [001] zone direction. Thus, more than 3300 lithium columns in the [001] projection were investigated. Among them, only ten or eleven lithium columns clearly showed a bright contrast with detectable intensity. A representative HAADF image for one of the bright lithium columns is presented in Figure S1 in the Supporting Information. Based on the image simulations (Figure 2), the observation of lithium columns with visible intensity should be plausible in both projections when lithium–iron exchange is 15% or more. However, the experimentally obtained HAADF images in the [001] projection show no detectable intensity in the lithium columns (Figure 3b), which contrasts with the images obtained in the [010] projection (Figure 3a). As the intensity of each atomic column in the HAADF images is critically dependent on the average *Z*, the absence of observable intensities in the lithium columns in the [001] projection directly demonstrates the strong preferential arrangement of antisite iron cations along the [010] direction.

An orientation-dependent arrangement of the antisite defects along the [010] direction is schematically described in Figure 4. For simplicity, one monolayer sublattice for the octahedral M1 sites of lithium ions (green) parallel to the (100) plane is shown without displaying the iron cations in the M2 sites. As depicted in the two-dimensional [100] projection (Figure 4a) and its three-dimensional configuration (Figure 4b), the antisite iron ions (red) are preferentially arranged along the *b* axis and are not randomly dispersed among the M1 sites. As the M1 octahedral sites in the $LiFePO_4$ structure are edge-sharing with each other along the [010] direction (Figure 4a), their shape is distorted to minimize the electrostatic repulsion between the adjacent lithium cations. On the other hand, if more than two cations of iron are exchanged, and are consecutively placed in the neighboring M1 sites, a significant repulsion is expected to occur between the neighboring iron cations. This situation is structurally unfavorable and induces instability to the edge-sharing M1 octahedral site. Thus, a consecutive arrangement of the exchanged iron cations would not commonly be present in the lattice, although they be preferentially arranged along the *b* axis.

It is now accepted that the ordered cation partitioning in $LiFePO_4$ results in remarkable orientation-dependent variation in the transport behavior of the lithium ions,[12] suggesting that the lowest activation barrier lies along the *b* axis.[12a,e,f] Thus, to achieve fast lithium intercalation, the distribution of antisite iron ions in the M1 sites needs to be controlled during synthesis of $LiFePO_4$ crystals. Assuming that there is a constant number of antisite iron cations in a crystal, if the iron cations are distributed in a homogeneous manner (Supporting Information, Figure S2a), they may block lithium transport

along the fastest diffusion path of the *b* direction, thereby resulting in confinement of the overall effective lithium mobility during the intercalation reaction. By contrast, such blockage by antisite iron ions can be avoided in most of the lithium columns if they are aggregated into just a few columns; in particular, by forming a one-dimensional configuration along the *b* axis (Supporting Information, Figure S2b). Therefore, based on direct observations, the present study shows that the $LiFePO_4$ crystals doped with niobium at a low concentration can have significant structural advantage for attaining high rate capability cathodes in rechargeable batteries[6c] by adjusting an atomic-scale defect array.

In summary, we have successfully synthesized niobium-doped $LiFePO_4$ crystals and have elucidated a local configuration of antisite iron ions in the M1 sites of the crystals through sensitive imaging of individual atom columns using aberration-corrected STEM and image simulations. The locally aggregated exchanged iron ions have been arranged preferentially along the *b* axis in the lattice, showing notable one-dimensional local clustering. This atomic-scale analysis suggests that the distribution of antisite defects in $LiFePO_4$ can be adjusted for improved lithium ion transport.

Experimental Section

Synthesis of $LiFePO_4$ and sample preparation: Niobium-doped $LiFePO_4$ samples were prepared using high-purity lithium carbonate (Li_2CO_3, 99.99%, Aldrich), iron oxalate dihydrate ($Fe^{II}C_2O_4{\cdot}2H_2O$, 99.99%, Aldrich), and ammonium dihydrogenphosphate ($NH_4H_2PO_4$, 99.999%, Aldrich). Niobium ethoxide ($Nb^{V}(OC_2H_5)_5$, 99.9%, Alfa Aesar; 4 mol%;) was also added as a dopant. A stoichiometric mixture of the powder of the starting materials and the dopant was milled in acetone for 24 h using zirconia ball mill. The dried slurry was calcined at 350 °C for 5 h in flowing high-purity argon (99.999%, 400 standard cubic centimenters per minute). Dense pellets pressed with the calcined powder for STEM observation were also sintered at 750 °C for 5 h in the same Ar atmosphere to avoid the exposure to moisture and oxygen. STEM specimens were prepared by mechanical grinding to a thickness of 80 μm, dimpling to a thickness of less than 10 μm and ion-beam thinning for electron transparency.

HAADF-STEM and image simulations: Atomic-resolution *Z*-contrast HAADF images were taken using a scanning transmission electron microscope (JEM-2100F, JEOL, Japan) at 200 kV with a spherical aberration corrector (CEOS GmbH, Germany). The size of an electron probe was about 1.2 Å. The collection semi-angles of a HAADF detector were adjusted from 73 to 195 mrad to use large-angle elastic scattering of electrons for *Z*-sensitive images. The obtained raw images were filtered to eliminate background noise using 2D difference filters (HREM Research Inc., Japan). The thickness of the observed regions in each sample was about 20 nm, as measured from the intensity ratio between the first plasmon-loss and the zero-loss peaks in the electron energy loss spectra. Image simulations based on the multislice method were performed using WinHREM. The intensity in ADF images was calculated by summing up the scattered electrons with collection semi-angles of 60 to 200 mrad. The effect of thermal vibration of atoms is included during the simulation based on the Weikenmeier–Kohl scattering factor.

Received: July 19, 2008
Published online: December 9, 2008

Keywords: antisite defects · crystal engineering · electron microscopy · solid-state structures

[1] a) S. M. Sze, *Semiconductor Devices, Physics and Technology*, Wiley, New York, **1985**, chaps. 1–2; b) D. J. Norris, A. L. Efros, S. C. Erwin, *Science* **2008**, *319*, 1776–1779.
[2] a) E. Mamontov, T. Egami, R. Brezny, M. Koranne, S. Tyagi, *J. Phys. Chem. B* **2000**, *104*, 11110–11116; b) F. Esch, S. Fabris, L. Zhou, T. Montini, C. Africh, P. Fornasiero, G. Comelli, R. Rosei, *Science* **2005**, *309*, 752–755.
[3] a) C. L. Jia, M. Lentzen, K. Urban, *Science* **2003**, *299*, 870–873; b) J. Mannhart, D. G. Schlom, *Nature* **2004**, *430*, 620–621.
[4] a) G. Hammerl, A. Schmehl, R. R. Schulz, B. Goetz, H. Bielefeldt, C. W. Schneider, H. Hilgenkamp, J. Mannhart, *Nature* **2000**, *407*, 162–164; b) J. P. Buban, K. Matsunaga, J. Chen, N. Shibata, W. Y. Ching, T. Yamamoto, Y. Ikuhara, *Science* **2006**, *311*, 212–215; c) Y. Sato, J. P. Buban, T. Mizoguchi, N. Shibata, M. Yodogawa, T. Yamamoto, Y. Ikuhara, *Phys. Rev. Lett.* **2006**, *97*, 106802.
[5] a) C. Wolverton, A Zunger, *Phys. Rev. B* **1998**, *57*, 2242–2252; b) C. Pouillerie, E. Suard, C. Delmas, *J. Solid State Chem.* **2001**, *158*, 187–197; c) Z. Lu, L. Y. Beaulieu, R. A. Donaberger, C. L. Thomas, J. R. Dahn, *J. Electrochem. Soc.* **2002**, *149*, A778–A791; d) Y. Shao-Horn, S. Levasseur, F. Weill, C. Delmas, *J. Electrochem. Soc.* **2003**, *150*, A366–A373; e) K. Kang, Y. S. Meng, J. Breger, C. P. Grey, G. Ceder, *Science* **2006**, *311*, 977–980.
[6] a) A. K. Padhi, K. S. Nanjundaswamy, J. B. Goodenough, *J. Electrochem. Soc.* **1997**, *144*, 1188–1194; b) A. Yamada, S. C. Chung, H. Hinokuma, *J. Electrochem. Soc.* **2001**, *148*, A224–A229; c) S.-Y. Chung, J. T. Bloking, Y.-M. Chiang, *Nat. Mater.* **2002**, *1*, 123–128; d) M. S. Whittingham, Y. Song, S. Lutta, P. Y. Zavalij, N. A. Chernova, *J. Mater. Chem.* **2005**, *15*, 3362–3379.
[7] R. C. Evans, *An Introduction to Crystal Chemistry*, 2nd ed., Cambridge University Press, London, **1966**, chap. 11.
[8] a) J. J. Papike, M. Cameron, *Rev. Geophys. Space Phys.* **1976**, *14*, 37–80; b) L. M. Hirsch, T. J. Shankland, *Geophys. J. Int.* **1993**, *114*, 21–35; c) C. M. B. Henderson, K. S. Knight, S. A. T. Redfern, B. J. Wood, *Science* **1996**, *271*, 1713–1715.
[9] D. E. Jesson, S. J. Pennycook, *Proc. R. Soc. London Ser. A* **1993**, *441*, 261–281.
[10] a) P. E. Batson, N. Dellby, O. L. Krivanek, *Nature* **2002**, *418*, 617–620; b) P. D. Nellist, M. F. Chisholm, N. Dellby, O. L. Krivanek, M. F. Murfitt, Z. S. Szilagyi, A. R. Lupini, A. Borisevich, W. H. Sides Jr. , S. J. Pennycook, *Science* **2004**, *305*, 1741; c) D. A. Muller, L. Fitting Kourkoutis, M. Murfitt, J. H. Song, H. Y. Hwang, J. Silcox, N. Dellby, O. L. Krivanek, *Science* **2008**, *319*, 1073–1076; d) W. D. Pyrz, D. A. Blom, T. Vogt, D. J. Buttrey, *Angew. Chem.* **2008**, *120*, 2830–2833; *Angew. Chem. Int. Ed.* **2008**, *47*, 2788–2791.
[11] S.-Y. Chung, S.-Y. Choi, T. Yamamoto, Y. Ikuhara, *Phys. Rev. Lett.* **2008**, *100*, 125502.
[12] a) D. Morgan, A. Van der Ven, G. Ceder, *Electrochem. Solid-State Lett.* **2004**, *7*, A30–A32; b) L. Laffont, C. Delacourt, P. Gibot, M. Y. Wu, P. Kooyman, C. Masquelier, J. M. Tarascon, *Chem. Mater.* **2006**, *18*, 5520–5529; c) G. Chen, X. Song, T. J. Richardson, *Electrochem. Solid-State Lett.* **2006**, *9*, A295–A298; d) R. Amin, P. Balaya, J. Maier, *Electrochem. Solid-State Lett.* **2007**, *10*, A13–A16; e) S.-I. Nishimura, G. Kobayashi, K. Ohoyama, R. Kanno, M. Yashima, A. Yamada, *Nat. Mater.* **2008**, *7*, 707–711; f) J. Li, W. Yao, S. Martin, D. Vaknin, *Solid State Ionics* **2008**, 179, 2016-2019.

